nature communications

Article

https://doi.org/10.1038/s41467-025-59795-y

Rhodopsin from *Haloquadratum walsbyi* is a light-driven magnesium transporter

Received: 29 February 2024

Accepted: 4 May 2025

Published online: 14 May 2025

Check for updates

Ling-Ning Ko, Guo Zhen Lim, Jui-Chien Chen, Ta Ko, Guan-Yi Li & Chii-Shen Yang

The functionally unknown Middle rhodopsin (HwMR) is a microbial rhodopsin (mRho) identified in *Haloquadratum walsbyi*, an archaeon that thrives in a 2 M $MgCl_2$ environment harmful to most other microorganisms. HwMR shares conserved and functionally critical residues with both bacteriorhodopsin (BR), a proton pump, and sensory rhodopsin II (SRII), which mediates phototaxis, even though HwMR exerts neither function. We previously reported HwMR as a unique mRho found to associate with Mg^{2+}. Here, we show that HwMR can sense environmental Mg^{2+} concentration via the D84 residue according to characteristic maximum absorption wavelength shift, photocycle kinetics, and Mg^{2+} titration assay. X-ray crystallography of the wild-type HwMR and its D84N mutant produced two HwMR atomic structure models. Omit maps analysis of the wild-type HwMR model revealed D84 as a Mg^{2+} binding site. On the cytoplasmic side, omit maps also revealed Mg^{2+} association with T216. Both Mg^{2+} sites were absent in the D84N mutant. A cell-based light-driven conductivity assay provided evidence to propose that HwMR is an inward magnesium transporter, with D84 as the primary binding site and T216 as the transportation stabilizing site. A sequential model was proposed to illustrate Mg^{2+} transportation in HwMR.

Rhodopsins, a class of photosensing proteins consisting of seven helices with a Schiff base linked retinal chromophore, are ubiquitously present across various organisms, both prokaryotes and eukaryotes. Rhodopsins are classified into Type I and Type II based on their functions and retinal conformation. Microbial rhodopsin (mRho) is categorized as Type I rhodopsin, typically retaining all-*trans* retinal in darkness. Type II rhodopsin comprises 11-cis retinal-bound rhodopsins, such as rhodopsin-like G protein-coupled receptors (GPCRs) found in mammals. Two main functions identified in Type I rhodopsin were light-driven ion transportation in bacteriorhodopsin (BR)[1] and halorhodopsin (HR)[2], and light-trigger phototaxis changes mediated by sensory rhodopsins (SRs)[3].

Haloquadratum walsbyi, characterized by its distinctive square-shaped morphology, demonstrated remarkable survival capabilities under high magnesium ion concentration, approximately 2 M $MgCl_2$[4], which harmed other haloarchaea. In 2006[5], the total genome study unveiled the presence of three mRhos in *H. walsbyi*, including bacteriorhodopsin (HwBR), halorhodopsin (HwHR), and middle rhodopsin (HwMR). While both HwBR and HwHR are functionally known, the function of HwMR has remained elusive since its discovery. By investigating their optical properties, we observed that HwBR exhibited tolerance to extremely low pH values[6], enabling the outward pumping of protons under such acidic conditions. HwHR served as a chloride pump with a high affinity for chloride ions[7].

Recently, we were committed to exploring the distinct features of HwMR and reported its unique properties associated with Mg^{2+}[8]. These properties included Mg^{2+}-dependent shifts in maximum absorbance (Abs-max) and kinetics changes in its photocycle. The residues located at the C-terminus impacted the formation of the M-state, a signaling intermediate state in the photocycle common among mRhos. Another important finding was regarding an aspartate residue, D84, known as a counterion positioned above the retinylidene Schiff base

Department of Biochemical Science and Technology, College of Life Science, National Taiwan University, Taipei, Taiwan, ROC.
e-mail: chiishen@ntu.edu.tw

on helix G. Our results hinted at the critical role of D84 in mediating the Mg^{2+} association in HwMR. Upon mutation of this residue, the sensitivity of HwMR towards cation concentrations was severely affected. In brief, altering concentrations of different cation ion species caused drastic Abs-max shifts and influenced the photocycle kinetics of HwMR.

Despite the adverse effects of excessive Mg^{2+} to most microorganisms, Mg^{2+} remains indispensable for maintaining regular cellular functions. Several Mg^{2+} channels[9] and transporters[10,11] exist naturally in archaea and eubacteria. The CorA family[10,11] characterized by conserved motifs and regulatory mechanisms, has been commonly studied. An example is the archaeal CorA from *Methanocaldococcus jannaschii* (MjCorA). It displayed a homopentameric composition[12] and revealed a distinctive groove at the N-terminus, which comprised eight aspartate and glutamate residues, serving as a region for Mg^{2+} accumulation. Additionally, a T264-ring formed from each monomer, which acted as a selectivity filter due to their hydroxyl groups. Besides these two specific regions, MjCorA exhibited other critical structure elements that regulate Mg^{2+} flux, such as the GMN motif and the hydrophobic lock.

Here, we report the atomic structures of the wild-type HwMR at a resolution of 2.5 Å and its D84N mutant at 2.9 Å. To understand the impact of this mutation, structural differences between D84 (wild-type) and N84 (mutant) were examined. According to omit maps, two distinct regions were determined as potential sites for Mg^{2+} binding: the space between D84 and D213 and between T216 and Y185. We observe that the D84N mutation eliminated the Mg^{2+} in these two binding sites and altered the optical properties of HwMR, as well as its photocycle kinetics. The mutation of D84N significantly disrupted the Mg^{2+} binding affinity of HwMR, as evidenced by Mg^{2+}-titration measurements. Together with light-dependent extracellular conductivity change measurements, we propose a model demonstrating the inward Mg^{2+} transporting mechanism in HwMR via the critical residues. This process is initiated with magnesium ions interacting with the ion selector, D84, stabilizing at the T216 residue and proceeding through HwMR into the cellular interior.

Results

The discovery of magnesium association in HwMR

Like light-driven proton-pumping bacteriorhodopsins, HwMR possesses a pair of conserved aspartic acid residues, D84 and D95, corresponding to D85 and D96 in HsBR from *Halobacterium salinarum* on helix C (Fig. 1a). In addition, it has a unique threonine residue, T216, which is highly conserved among archaeal sensory rhodopsins (SRs) like NpSRII from *Natronomonas pharaonis*. A series of single-point mutations at those residues were conducted to examine their functional importance in HwMR. Replacement of Asp84 with Asn, D84N-HwMR, to mimic a fully protonated counterion of the retinal Schiff base caused the largest blue shift in Abs-max (approximately 15 nm) in 2.0 M $MgCl_2$, compared to high NaCl and $CaCl_2$ conditions (Fig. 1c).

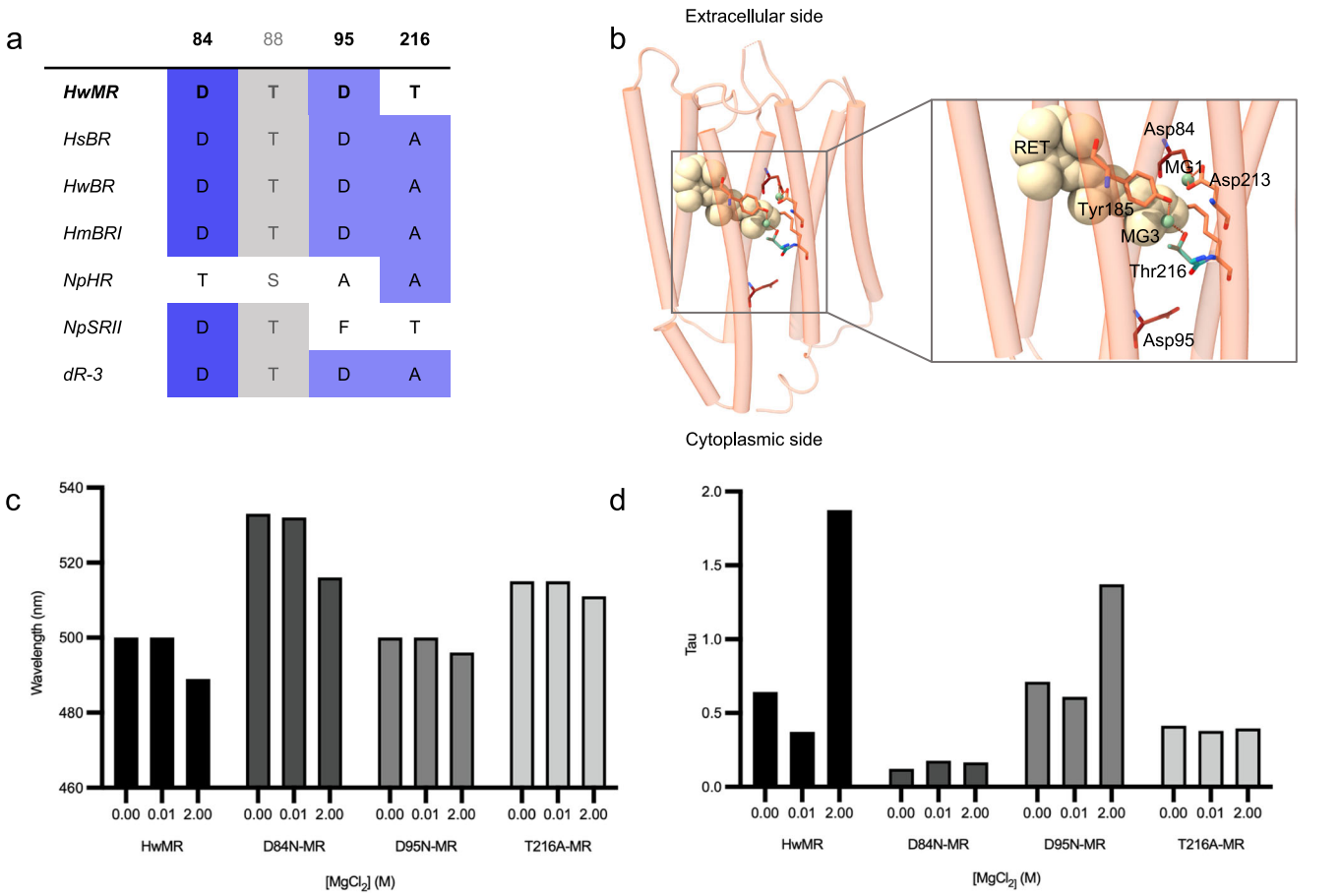

Fig. 1 | Optical properties of wild-type HwMR and its variants. a Sequence alignment of key residues in HwMR and other mRhos. Using HwMR as a reference, the sequence alignment was performed for several mRhos, including HsBR, HwBR, HmBRI, NpHR, NpSRII, and dR-3. The amino acid numbering is based on HwMR. See Supplementary Fig. 1 for the full sequence alignment. (PDB ID: 9JWS, 1C3W, 4QI1, 4PXK, 5ETZ, 1JGJ, and 4FBZ, respectively). **b** The wild-type HwMR structure displayed the conserved residues in red or blue sticks, including D84, D95, and T216 residues. **c** UV–Vis spectrophotometry was employed to measure the Abs-max shifts of wild-type HwMR and its variants under $MgCl_2$ concentrations from 0 to 2.0 M. **d** Photocycle of wild-type HwMR and variants under $MgCl_2$ concentrations from 0 to 2.0 M were conducted at specific ground-state wavelengths. Utilizing the one-phase decay, tau values were calculated to characterize the kinetics of the photocycle.

https://doi.org/10.1038/s41467-025-59795-y

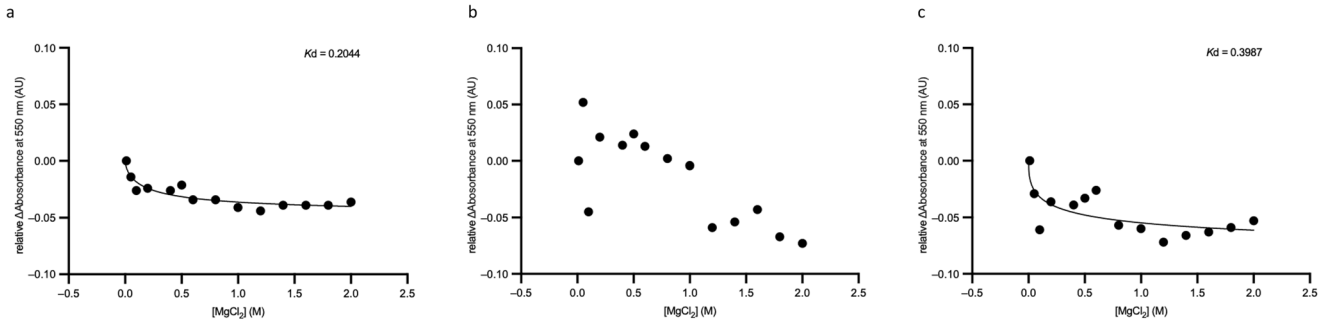

Fig. 2 | Mg^{2+}-binding affinity of wild-type HwMR and D84N mutant. The UV−Vis spectrum of **a** wild-type HwMR, **b** D84N and **c** T216A mutants were recorded under varying concentrations of $MgCl_2$ ranging from 0.01 to 2 M. The absorbances of proteins were normalized against 0.01 M $MgCl_2$ and plotted against $MgCl_2$ concentrations. The absorbance differences at 550 nm for wild-type HwMR and T216A mutant were fitted via the Hill equation. The Hill equation: Y=Bmax*X^h/ (Kd^h + X^h), where Kd represented the equilibrium dissociation constant. For the D84N mutant, the absorbance differences at 550 nm were fitted using linear regression without Kd calculations since the Hill equation was not applicable.

Furthermore, D84N-HwMR disrupted its Mg^{2+}-dependent photocycle seen in wild-type, causing a 10-fold increase in speed compared to wild-type HwMR (Fig. 1d) and bypassing the M-state regardless of surrounding cation concentrations[8].

The T216A-HwMR mutation caused a slight blue shift in the Abs-max (Fig. 1c) and disrupted its Mg^{2+}-dependent kinetics changes in photocycle under $MgCl_2$ concentrations ranging from 0.01 to 2.0 M (Fig. 1d). This suggests that T216 may influence the sensitivity of HwMR toward environmental Mg^{2+}.

The Abs-max of D95N-HwMR was similar to that of wild-type HwMR, approximately at 500 nm. In contrast, there was no significant Abs-max shift (Fig. 1c) under $MgCl_2$ concentrations ranging from 0.01 to 2.0 M, while this mutant exhibited Mg^{2+}-dependent changes in photocycle kinetics similar to the wild-type HwMR (Fig. 1d), with slower kinetics observed at higher $MgCl_2$ concentrations. This suggests that Asp95 does not directly affect the sensitivity to Mg^{2+} during the photocycle.

To further determine the Mg^{2+}-binding affinity, the absorbance differences at the characteristic 550 nm were plotted against $MgCl_2$ concentrations and fitted using the Hill equation[13] (Fig. 2, Supplementary Fig. 2). The dissociation constant (Kd) for wild-type HwMR (Fig. 2a) was 0.2044 M, whereas the D84N mutant altered the Mg^{2+}-binding affinity curve from biphasic to a simple linear regression, and the Kd could not be calculated (Fig. 2b). Interestingly, the T216A mutant (D84 not mutated) retained the biphasic affinity curve despite having a higher Kd of 0.3987 M (Fig. 2c).

These biochemical experiments provided clear evidence that HwMR exhibited sensitivity to Mg^{2+} ions. These findings suggest that D84 is the primary Mg^{2+} binding site in HwMR, while T216 may act as a transition or stabilizing site, potentially modulating Mg^{2+} sensitivity. D95 was shown to play a less significant role in optical properties and Mg^{2+} coordination during the photocycle, consistent with the conserved D96 proton donor in BRs[14]. To validate these findings, we conducted a structural analysis of wild-type and D84N-HwMR to confirm the Mg^{2+} binding sites and their configurations.

Crystal growing of HwMR proteins

In this study, both wild-type HwMR and the D84N mutant were purified and dialyzed under 10 mM $MgCl_2$ with 200 mM NaCl, 50 mM sodium acetate pH 5.5 (for wild-type) or pH 4.5 (for D84N), and 0.15% DM prior to lipid cubic phase (LCP) *in meso* crystallization[15]. Wild-type HwMR was grown in 200 mM lithium sulfate, 100 mM imidazole pH 8.0, and 30% PEG 400, resulting in flaky crystals (Supplementary Fig. 3c), resulting in insufficient diffraction data from single crystals on the c-axis. Consequently, diffraction data from multiple wild-type HwMR crystals were collected at the TPS 07 A micro-focus, variable beam-size beamline at NSRRC (Hsinchu, Taiwan) and merged by the KAMO program. We collected over three hundred wild-type HwMR micro-crystals, with only 101 providing usable diffraction data. These 101 crystals were clustered based on space group and amplitude information. Diffraction data were collected from multiple crystals using raster scanning at TPS 07A and processed with KAMO[16], followed by BLEND[17] to perform hierarchical clustering, grouping datasets based on similarities in unit-cell parameters to identify and reject outliers. The remaining 46 selected crystal diffraction data were then scaled and merged using XSCALE. The wild-type HwMR diffraction data were merged to obtain an overall resolution of 2.5 Å (Supplementary Table 1).

The D84N mutant was grown in 50 mM NaCl, 50 mM sodium citrate pH 5.5, and 15% PEG 400, and predominantly formed stick-shaped crystals (Supplementary Fig. 3c). The X-ray diffraction data from a single crystal of D84N mutant was collected via the TLS 15 A beamline of NSRRC. The D84N mutant crystal diffracted to 2.9 Å (Supplementary Table 1).

Overall structures of wild-type HwMR and its D84N mutant

Typical for microbial rhodopsins, the wild-type HwMR and D84N-HwMR structures contain seven transmembrane helices and all-*trans* retinal forming retinylidene Schiff base with residue K217 (Fig. 3). The Bravais lattice identified for wild-type HwMR was P21 21 21, accommodating two molecules within an asymmetric unit cell (Fig. 3a). In contrast, the Bravais lattice for the D84N mutant was P1 21 1, and four molecules were stacked in an asymmetric unit cell (Fig. 3b). Due to the detergent component in the protein purification conditions, the proteins displayed a monomeric conformation.

It is worth noting that the electron density maps in the BC-loop and C-terminal loop of the two structures are significantly weaker. The protein backbones that do not fit well into maps were excluded from the model.

D84 and T216 are the magnesium binding sites

By analyzing the Fo-Fc map of wild-type HwMR, we observed a positive omit map between residues D84 and D213 (Fig. 4a), indicating a putative ion binding site. Our functional analysis results from a severe Mg^{2+}-dependent Abs-max shift, the lack of Mg^{2+}-dependent photocycle kinetics (Fig. 1d) and the disrupted Mg^{2+} binding affinity caused by the D84N mutation (Fig. 2b) showed the significance of D84 residue on Mg^{2+} association, leading us to assign a Mg^{2+} ion between D84 and D213 in both chains of the wild-type model. The atomic distances between Mg^{2+} and the OD2 of D84 were 2.88 Å in chain A and 2.70 Å in chain B, respectively. We noticed that the assigned Mg^{2+} ions were slightly closer to the D213 residue, with atomic distances of 2.31 Å to OD1 and 2.35 Å to OD2 in chain A; 2.24 Å to OD1 and 2.77 Å to OD2 in chain B (Fig. 4b). The distances between Mg^{2+} and its neighboring residues were either comparable to or

https://doi.org/10.1038/s41467-025-59795-y

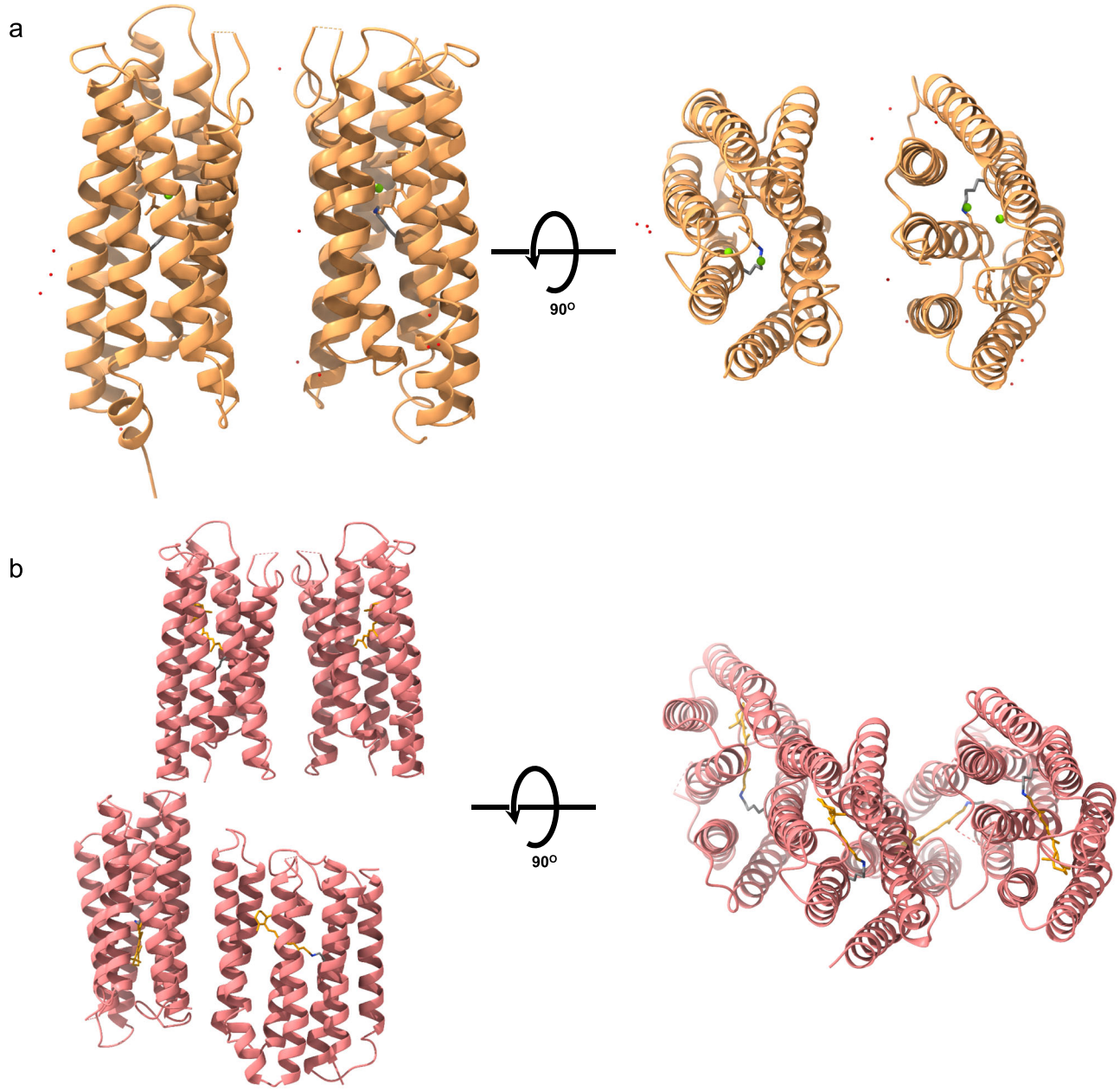

Fig. 3 | The overall structure and unique ligand bindings of wild-type HwMR and D84N mutant. a The side (left) and top views (right) of wild-type HwMR were visually represented as cartoon structures. The all-*trans* retinal and water molecules were labeled in yellow sticks and red spheres, respectively. Four magnesium ions (green spheres) were positioned within the wild-type HwMR structure. **b** The side (left) and top views (right) of D84N mutant visually represented as cartoon structures. The all-*trans* retinal was labeled in yellow sticks. Water molecules are not placed in structure with validation of PHENIX refinement program.

shorter than hydrogen-bond length[18], supporting that D84 is a Mg^{2+} binding site in HwMR.

We also discovered another positive omit map (Fo-Fc map) between T216 and Y185 in the wild-type model (Fig. 4c), with an atomic distance of 2.06 Å and 1.55 Å from T216 of chain A and chain B, respectively (Fig. 4d). Taken together, moderate Mg^{2+}-dependent Absmax shifts (Fig. 1c), disrupted Mg^{2+}-dependent photocycle and a decrease in Mg^{2+} binding affinity upon alanine substitution (T216A mutant) strongly suggest the involvement of T216 in Mg^{2+} association. The short atomic distance well within the range for ionic bond formation led us to propose T216 as a stabilizing site that accommodates Mg^{2+} ion transportation upon light-driven conformational change.

No omit map was observed around D95 in both chains of wild-type HwMR (Fig. 4e). This structural observation was in agreement with the results of optical property analysis and photocycle kinetic studies on D95N-HwMR, which showed weak interaction between D95 and Mg^{2+} ions.

In stark contrast, the D84N-HwMR mutant model lacks any positive omit map for ion assignment at neither position (between N84-D213 or the unmutated T216-Y185) (Fig. 5), further suggesting the significance of D84 in stabilizing the Mg^{2+} ion. When the negatively charged Asp was substituted with a neutral Asn, Mg^{2+} binding was not observed. It was worth mentioning that our biochemical and biophysical evidence (Figs. 1c, d, 2) strongly corroborates the structural significance of D84 in Mg^{2+} ion association and indicates that the D84N mutation likely eliminated the Mg^{2+} network present in the wild-type structure.

Exploring the putative magnesium transportation direction

The absence of Mg^{2+} association at both D84 and T216 in the D84N model, in conjunction with the established importance of these

https://doi.org/10.1038/s41467-025-59795-y

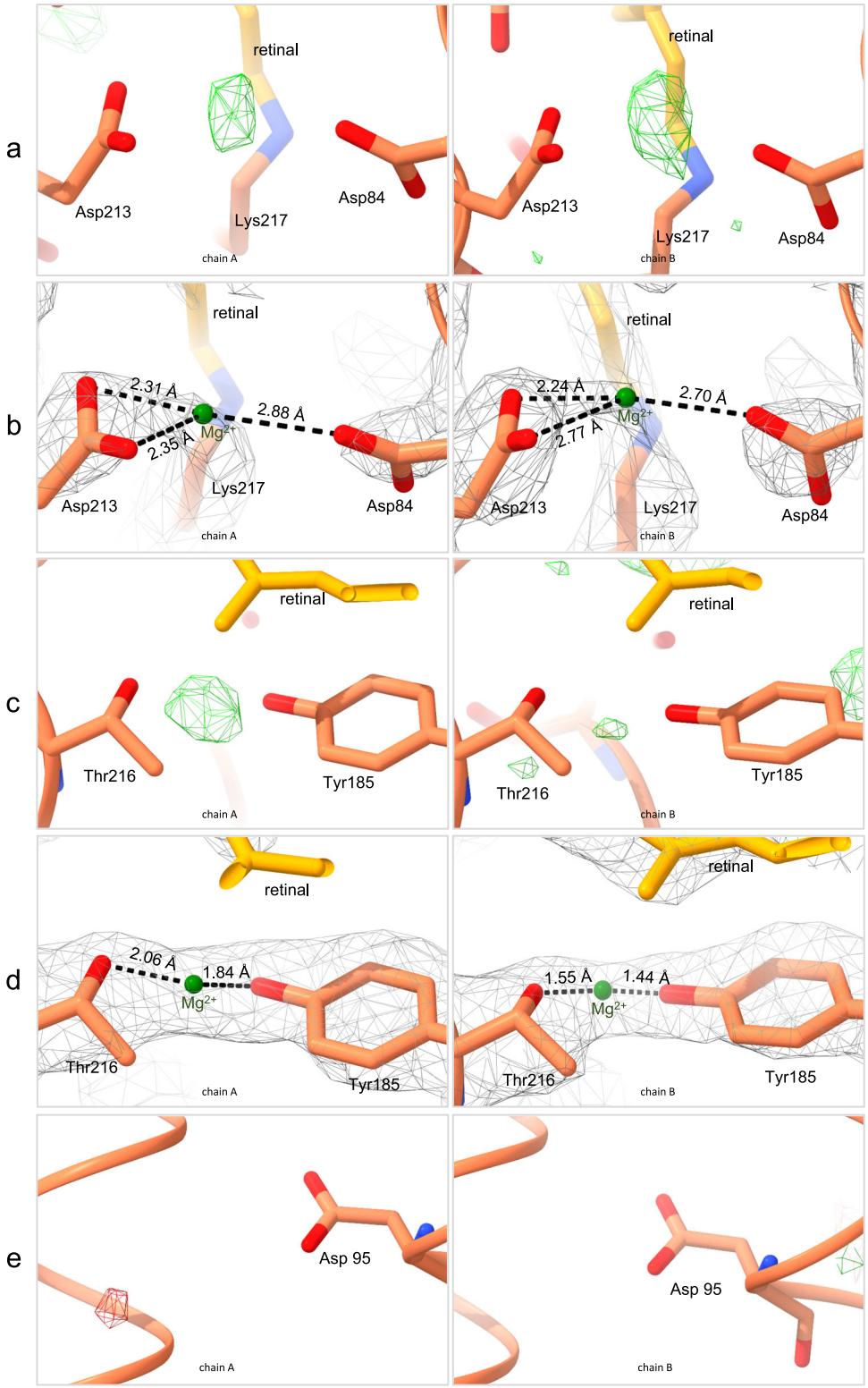

Fig. 4 | Omit map analysis of the wild-type HwMR structure. a Positive omit map (green mesh, contoured at 3.0 σ) between D84 and D213 in wild-type HwMR. **b** The distances between assigned Mg^{2+} to its neighboring residues. The distances are measured by ChimeraX. **c** Positive omit map (green mesh, contoured at 3.0 σ in chain A and at 2.0 σ in chain B) between T216 and Y185 in wild-type HwMR. **d** The distances between assigned Mg^{2+} to its neighboring residues. The distances are measured by ChimeraX. **e** No omit map is observed around D95 in wild-type HwMR. Electron density map (2Fo-Fc) is contoured as gray mesh at the level of 1.0*σ*.

residues in the optical and biochemical properties of HwMR, provides compelling evidence for Mg^{2+} transportation in HwMR. As there is no widely recognized method to directly measure the trace changes in Mg^{2+} across membranes, we indirectly assessed Mg^{2+} transport and its direction by measuring the light-induced whole-cell suspension conductivity changes in HwMR-expressing cells under Mg^{2+} enriched conditions. To validate the system, we expressed light-driven proton-pumping HwBR in *E. coli* as a control and detected a positive

https://doi.org/10.1038/s41467-025-59795-y

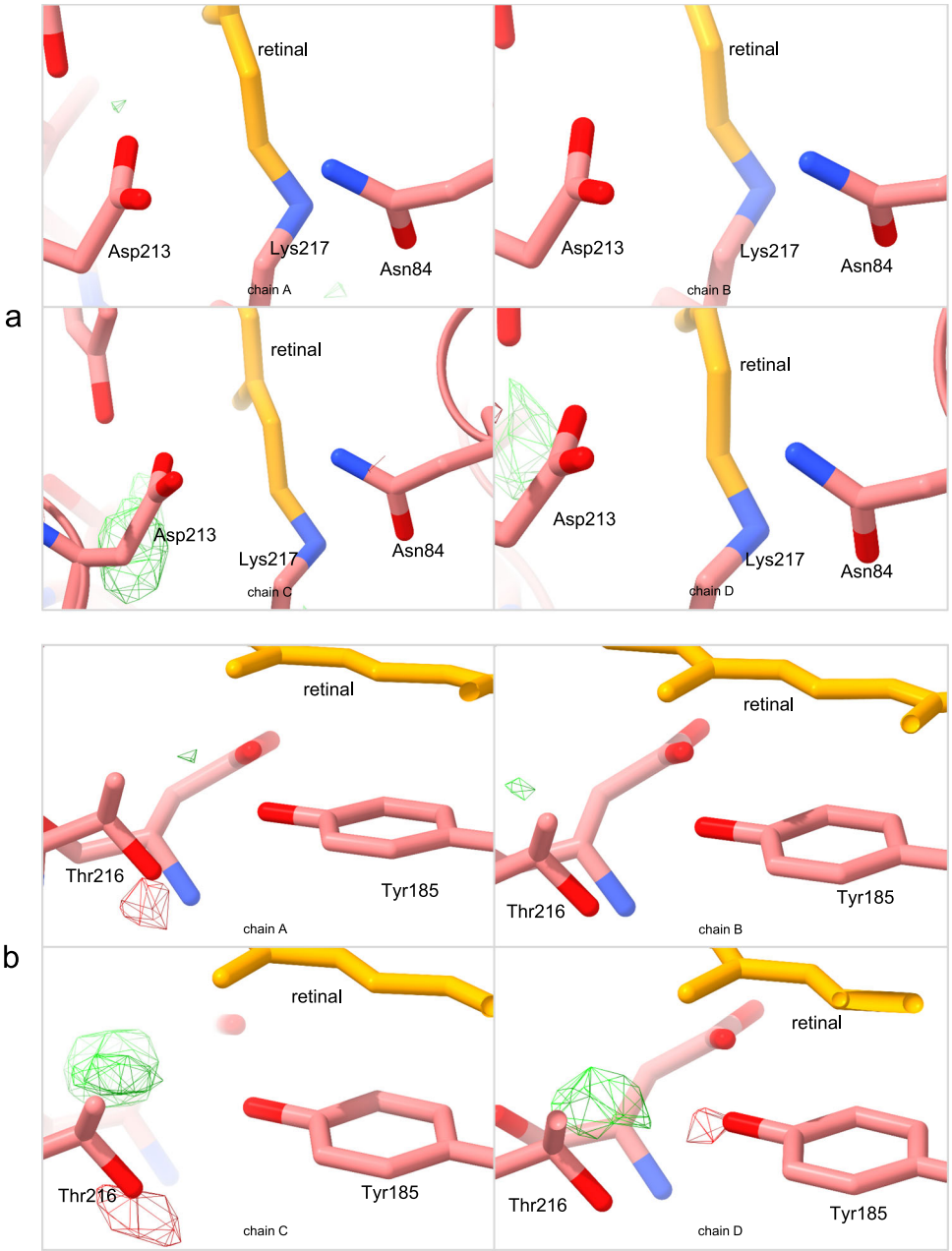

Fig. 5 | Omit map analysis of the D84N-HwMR structure. Omit map is contoured at 3.0σ as green (positive) mesh and red (negative) mesh. **a** Omit map is not observed between N84 and D213 in D84N-HwMR. **b** Omit map is not observed between T216 and Y185 in D84N-HwMR.

conductivity slope change upon light illumination (Fig. 6), indicating that the increase in overall extracellular conductivity caused by outward proton transportation was detectable.

We used the same approach and observed that *E. coli* cells expressing wild-type HwMR exhibited a negative conductivity slope change upon light illumination (Fig. 6), indicating a decrease in overall extracellular conductivity. Among the mutants, only cells expressing D84N-HwMR flip the conductivity slope change to positive. Those cells expressing D95N- or T216A-HwMR exhibited similar trends as the wild-type, showing negative conductivity slope changes.

Since the major ion species in the extracellular solution was Mg^{2+}, it is only logical to infer that the conductivity changes occurred due to Mg^{2+} ion transportation by HwMR across the *E. coli* plasma membrane. Moreover, the overall extracellular conductivity decreased with the activation of wild-type HwMR expressed in *E. coli* strongly suggests an inward Mg^{2+} transportation via HwMR. D84N was the only mutant that disrupted this transportation directionality, while substituting threonine to alanine in the T216A mutant retained the inward Mg^{2+} transportation tendency. These results and atomic structural analysis provide further evidence supporting the crucial role of D84 as the primary Mg^{2+} binding site, while the T216 serves as the stabilizing site for Mg^{2+} transportation.

Discussion

In this research, we present the structures of a light-driven Mg^{2+}-transporting microbial rhodopsin (mRho), including both its wild-type form and a functionally significant mutant. Being a mRho with two identities, having conserved residues from well-characterized BR and SRII, the function of HwMR remained a mystery for over a decade. Our recent study[8] discovered HwMR as the first Mg^{2+}-associated mRho, but critical binding and possible transportation mechanisms remain elusive. Our analysis of the wild-type HwMR and the D84N mutant crystal

https://doi.org/10.1038/s41467-025-59795-y

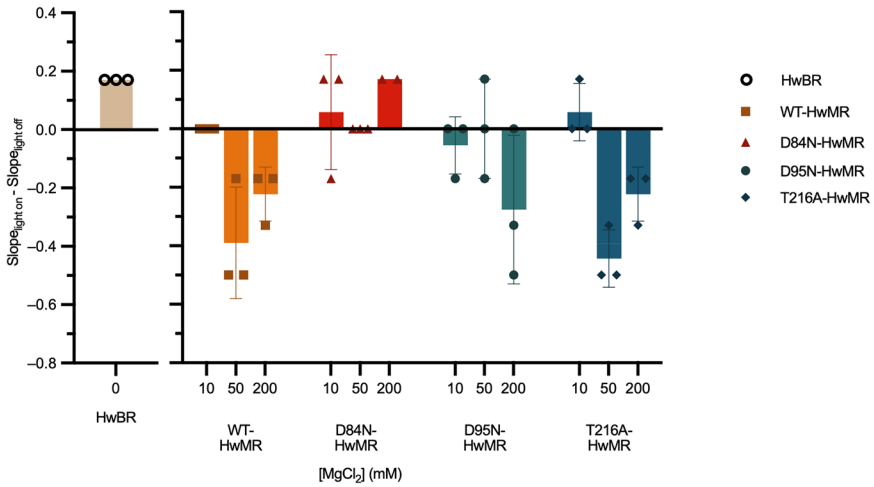

Fig. 6 | The conductivity changes of the whole cell expressing rhodopsins. The *E. coli* cell expressing wild-type HwMR (orange), D84N-HwMR (red), D95N-HwMR (teal), and T216A-HwMR (blue) were adjusted to OD_{600} of 20 and suspended in $MgCl_2$ solutions ranging from 10 to 200 mM supplemented with 10 mM $MgSO_4$, and 0.1 mM $CaCl_2$. Continuous real-time conductivity measurements under dark and a 3 W green LED illumination were taken with 60-second cycles to calculate conductivity slope changes. Conductivity slope change values are means ± s.e.m. (n = 3).

structures, supported by mutagenesis studies that investigate the roles of key residues in Mg^{2+}-dependent Abs-max shift (Fig. 1c), photocycle kinetics (Fig. 1d), spectral-based binding affinity (Fig. 2), allowed us to confirm previous reports of Mg^{2+} association with HwMR and further identified D84 as the primary Mg^{2+} binding sites and T216 as the stabilizing site.

We observed a sequence of events wherein magnesium ions initially accessed the D84 residue, were subsequently stabilized at T216, and proceeded through the HwMR structure. We can infer from the conductivity measurements of the loss-of-function mutant, D84N-HwMR, on whole cells (Fig. 6) that inward Mg^{2+} transportation is facilitated via residue D84. Based on our findings, we proposed a model illustrating the magnesium ion transporting mechanism in HwMR (Fig. 7). In this model, D84 regulates ion species accessibility and facilitates inward Mg^{2+} transportation, while T216 residue stabilizes Mg^{2+} in this region during the transitional state, and D95 acts as an associator, possibly without directly engaging Mg^{2+}. Furthermore, this transportation mechanism is Mg^{2+}-sensitive. The slower photocycle kinetics of HwMR protein under higher extracellular $MgCl_2$ concentrations represent a dynamic regulated mechanism in response to varying intracellular Mg^{2+} levels during the inward Mg^{2+} transportation (Fig. 1d). The physiological implication of this regulation is worth further investigation.

The importance of the retinal Schiff base counterion has long been the key highlight in mRho studies. Three amino acids at conserved positions on the helix C have been identified as the characteristic motif that can correlate to the mRho functions[19]. In HsBR, residues D85, T89, and D96 comprise the well-known DTD motif, which conducts the counterion switch with retinal to facilitate proton transportation. Similarly, a DTF motif was found in sensory rhodopsins, a TSA motif in the chloride-pumping HR, while an NDQ motif is identified in the sodium pump, *Krokinobacter* rhodopsin 2 (KR2)[20,21].

HwMR was initially thought to be a variant of BR due to the presence of a DTD motif identical to that of typical BR[22]. However, sequence alignment revealed that HwMR possesses a threonine residue at a position unique to SR, unlike other ion-transporting mRhos that typically have an alanine at this position (Fig. 1a, Supplementary Fig. 1). It was soon discovered that HwMR does not pump protons like BR, as photocurrents of purified HwMR proteins or whole-cell *E. coli* expressing HwMR were undetectable. Our previous studies[8] demonstrated that HwMR, a unique microbial rhodopsin (mRho) associated with magnesium ions, exhibited a slower photocycle compared to HwBR. Additionally, the presence of magnesium ions caused changes in the micro-environments near the retinal binding pocket. This leads to the Abs-max shifts and photocycle kinetic changes under varying magnesium ion concentrations, demonstrating the magnesium sensitivity of HwMR (Fig. 1). Despite a previous study based on solid-state nuclear magnetic resonance spectroscopy[23] suggesting that HwMR presented various retinal configurations in the dark, such as all-*trans*, 11-*cis*, and 13-*cis* forms, the all-*trans* retinal isoform best fits in our density map for both wild-type HwMR and its D84N mutant models (Supplementary Fig. 4).

Comparing the coulombic electrostatic potential of the assigned Mg^{2+} from D84 (in the wild-type HwMR model) and N84 (in the D84N-HwMR mutant model) revealed that the fully protonated N84-induced electrostatic repulsion (Supplementary Fig. 5a, b) hindering the accommodation of Mg^{2+} in this region. This phenomenon conformed to the comparison between HwBR and its D93N mutant (Supplementary Fig. 5c, d), as well as HsBR and its D85S mutant (Supplementary Fig. 5e, f).

This study provided the structural evidence of Mg^{2+} binding in HwMR. We proposed an inward transportation pathway by identifying critical residues that facilitate the Mg^{2+} transportation, supported by mutagenesis investigations via optical and biochemical experiments. These discoveries paved the way for further elucidation of the unique physiological role HwMR plays in the tolerance of magnesium-rich environments.

Methods

Bacterial strains and plasmid construction

Escherichia coli DH5α cells were utilized in the cloning process, while protein expression employed *E. coli* C43(DE3) cells. The HwMR genes, synthesized by Genomics Co. (Taipei, Taiwan), were tailored with an NcoI restriction enzyme cutting site preceding the start codon and an XhoI restriction enzyme cutting site following the stop codon. The DNA fragment was treated with restriction enzymes and was integrated into a pET-21d vector pre-treated with NcoI and XhoI. The site-directed mutagenesis was executed following the instruction manual accompanying the QuikChange Lightning Site-Directed Mutagenesis Kit (Agilent Technologies, headquartered in Santa Clara, CA).

Protein expression in *E. coli* and purification

A transformed *E. coli* C43(DE3) colony was cultured overnight in LB medium with 50 μg/ml ampicillin at 37 °C. To scale up protein

https://doi.org/10.1038/s41467-025-59795-y

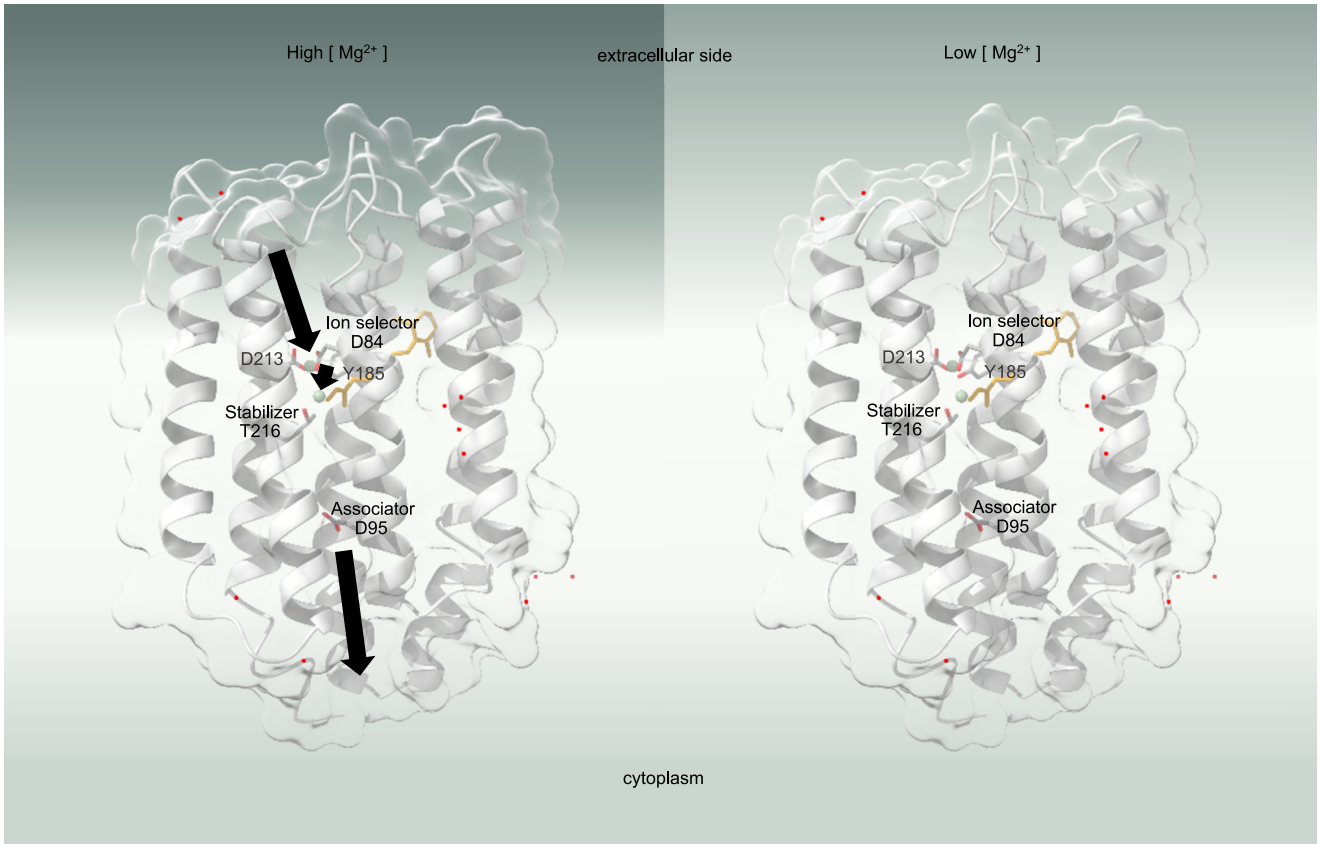

Fig. 7 | The model of the Mg^{2+} transporting mechanism. Critical residues, D84, D95, and T216, were depicted in sticks, while the all-*trans* retinal was presented in yellow. The magnesium ions and water molecules were displayed as green and red spheres, respectively. The background color was dark to light green, symbolizing a spectrum of magnesium ion concentrations from high to low. Black arrows showed the Mg^{2+} transportation route, with bolder arrow widths indicating the higher amount of Mg^{2+} transported and the corresponding slower transportation speed (photocycle kinetics).

expression, a 1:50 dilution of the overnight culture was incubated in a fresh LB/ampicillin medium at 37 °C. IPTG (isopropyl β-D-1-thiogalactopyranoside, final concentration 1.0 mM) and all-*trans* retinal (final concentration 5.0–10.0 μM) were added at an OD_{600} of 0.4–0.6 for induction, followed by 4 h of dark incubation. Cells were harvested at 6759 × *g*, 4 °C for 10 min (Hitachi CR-21, R10A3), resuspended in buffer A (4.0 M NaCl, 50 mM Tris pH 7.8, 14.7 mM 2-mercaptoethanol, 0.2 mM PMSF), and sonicated (S-3000; MISONIC). After 38,886 × *g*, 4 °C for 10 min (Hitachi CR-21, R20A2) for debris removal, using ultracentrifugation (Hitachi CP 80WX) at 237,662 × *g*, 4 °C for 1 h to acquire membrane fraction. The sediment was dissolved in buffer B (4.0 M NaCl, 50 mM Tris pH 7.8, 2% DDM) at 4 °C for at least 12 h and centrifuged (38,886 × *g*, 4 °C for 45 min) to obtain the detergent-soluble fraction. Ni-NTA affinity purification was performed by incubating the detergent-soluble solution with Ni-NTA agarose (20 mM imidazole, 4 °C for 4 h) and subsequent chromatography column washing using buffer C (200 mM NaCl, 50 mM Tris pH 7.8, 0.15% DM, 50 mM imidazole). Elution was achieved with buffer D (200 mM NaCl, 50 mM Tris pH 7.8, 0.15% DM, 250 mM imidazole). Purified proteins were concentrated and exchanged into buffer E (200 mM NaCl, 10 mM $MgCl_2$, 50 mM sodium acetate pH 5.5, 0.15% DM) using a 30 kDa cutoff protein concentrator (Millipore, Amicon).

Lipid cubic phase preparation and crystallization

To reconstitute the lipid cubic phase (LCP), wild-type HwMR and D84N mutant concentrations were adjusted to 30–40 mg/ml after purification using a Superdex200 Increase 10/300 GL column, followed by dialysis in Buffer E (200 mM NaCl, 10 mM $MgCl_2$, 50 mM sodium acetate pH 5.5, and 0.15% DM) for wild-type HwMR and Buffer F (200 mM NaCl, 10 mM $MgCl_2$, 50 mM sodium acetate pH 4.5, and 0.15% DM) for D84N-HwMR. Using a method described in previous studies[15,24], two 250-μl syringes connected via a syringe coupler were employed. The target proteins were evenly mixed with 1-Oleoyl-rac-glycerol (monoolein) in a 40:60 volume ratio for approximately 5 minutes. The resulting homogeneous mixtures were then loaded into a 10-μl microsyringe, with 0.2 μl of LCP injected into each chamber of the crystallization plate. Then the LCP was covered by 2 μl of precipitant reservoirs: wild-type HwMR growing in 200 mM Lithium sulfate, 100 mM imidazole pH 8.0, and 30% PEG 400, and D84N-HwMR growing in 50 mM NaCl, 50 mM sodium citrate pH 5.5, and 15% PEG 400. The crystallization plates were securely sealed and then incubated in darkness for about 30 days at 16 or 20 °C. Finally, the protein crystals were soaked in 20% glycerol as a cryoprotection before freezing and X-ray exposure.

X-ray diffraction data collection

The X-ray diffraction data for wild-type HwMR were acquired at the TPS 07A beamline within the National Synchrotron Radiation Research Center (NSRRC) in Hsinchu, Taiwan. The diffractions from numerous crystals were collected using raster scanning at TPS 07A and utilized KAMO[16] and BLEND[17] to merge and perform unit-cell-based hierarchical clustering analysis. Outliers were identified and rejected from the data prior to scaling and merging with XSCALE. For the X-ray diffraction data of D84N-HwMR, data collection took place at TLS 15A of NSRRC. The data from the single crystal were processed using HKL2000[25]. For the molecular replacement of wild-type HwMR and D84N mutant, respective initial models were generated using AlphaFold2 as their templates[26]. The molecular replacement and structure

refinement were conducted using PHENIX[27], CCP4[28], and COOT[29]. UCSF ChimeraX[30] was used to analyze and compare features between the HwMR wildtype and the mutant proteins.

Sequence alignment

The multiple sequence alignment was conducted using ClustalW on Ugene (Unipro) for the following proteins: HwMR, HsBR, HwBR, HmBRI, NpHR (halorhodopsin from *Natronomonas pharaonis*), NpSRII (Sensory rhodopsin II from *N. pharaonis*), and dR-3 (deltarhodopsin-3 from *Natrinema thermotolerans*). The UniProt accession numbers correspond to each protein, respectively: Q18DH5, P02945, G0LFX8, Q5UXY6, A0A1U7EU03, P42196, and I4DST7.

UV–visible spectroscopy

Following purification, the target proteins were dialyzed into solutions containing varied concentrations of specific ions. UV-visible spectra were captured using a U-1900 spectrophotometer (Hitachi) while maintaining a constant temperature of 298 K. Instrument settings were standardized, employing a fixed slit-width of 4.0 nm and a consistent scan speed of 400 nm/min.

Flash-laser induced photocycle measurements

Flash-absorbance changes induced by an Nd-YAG laser (532 nm, 6.0 ns pulse, 40 mJ) were measured using a specialized laboratory-constructed laser cross-beam flash spectrometer. Purified proteins were calibrated to a normalized absorbance value of 0.5 at their respective Abs-max. The transient absorbance changes were recorded at the Abs-max of their corresponding ground state. The observed curves displayed the dynamic alterations in absorbance levels at specific target wavelengths driven by a green laser (λ_{ex} = 532 nm). These changes elucidate the loss and subsequent recovery of absorbance at the defined wavelengths.

Magnesium titration assay

To determine the magnesium-binding affinity, using a methodology described in a prior study[7], the purified wild-type HwMR and D84N mutant were adjusted to varying $MgCl_2$ concentrations ranging from 0.01–2 M including 50 mM MES pH 5.8 and 0.02% DDM. The UV-visible spectrum was recorded and normalized across different $MgCl_2$ concentrations. Subsequently, the absorption changes observed in wild-type HwMR and D84N mutant were baselined with that of 0.01 M $MgCl_2$, and these changes were then plotted against $MgCl_2$ concentrations and subjected to fitting using the Hill equation. The Hill equation: Y = Bmax*X^h/ (Kd^h + X^h), where Kd represents the equilibrium dissociation constant.

Light-driven whole-cell conductivity measurements

E. coli cells (C43 strain) expressing wild-type, D84N-, D95N- and T216A-HwMR were prepared at an optical density of 20 and suspended in $MgCl_2$ solutions ranging from 10 to 200 mM supplemented with 10 mM $MgSO_4$ and 0.1 mM $CaCl_2$. Following cell preparation, real-time measurements of conductivity values in the extracellular solutions were performed. The cells were illuminated with a 3 W green LED during light illumination. The slope changes in conductivity values during darkness and illumination were calculated.

Reporting summary

Further information on research design is available in the Nature Portfolio Reporting Summary linked to this article.

Data availability

The atomic coordinates have been deposited in the Protein Data Bank (PDB) under accession codes 9JWS (wild-type HwMR); and 8XHW (D84N-HwMR). The PDB accession codes for previously published protein structures were PDB ID: 1C3W, 4QI1, 4PXK, 5ETZ, 1JGJ, and 4FBZ. The UniProt protein accession number for this study is Q18DH5 (HwMR). The source data underlying Figs. 1c, d, 2, 6 and Supplementary Fig. 2a-b, 3a, b are provided as a Source Data file. Source data are provided with this paper.

References

1. Lanyi, J. K. Proton translocation mechanism and energetics in the light-driven pump bacteriorhodopsin. *Biochim. Biophys. Acta* **1183**, 241–261 (1993).
2. Varo, G. et al. Light-driven chloride ion transport by halorhodopsin from Natronobacterium pharaonis. 1. The photochemical cycle. *Biochemistry* **34**, 14490–14499 (1995).
3. Schegk, E. S. & Oesterhelt, D. Isolation of a prokaryotic photoreceptor: sensory rhodopsin from halobacteria. *EMBO J.* **7**, 2925–2933 (1988).
4. Bolhuis, H., Poele, E. M. & Rodriguez-Valera, F. Isolation and cultivation of Walsby's square archaeon. *Environ. Microbiol.* **6**, 1287–1291 (2004).
5. Bolhuis, H. et al. The genome of the square archaeon Haloquadratum walsbyi: life at the limits of water activity. *BMC Genom.* **7**, 169 (2006).
6. Fu, H. Y. et al. Insight into a single halobacterium using a dual-bacteriorhodopsin system with different functionally optimized pH ranges to cope with periplasmic pH changes associated with continuous light illumination. *Mol. Microbiol.* **88**, 551–561 (2013).
7. Fu, H. Y. et al. Ser(262) determines the chloride-dependent colour tuning of a new halorhodopsin from Haloquadratum walsbyi. *Biosci. Rep.* **32**, 501–509 (2012).
8. Ko, L. N. et al. HwMR is a novel magnesium-associated protein. *Biophys. J.* **121**, 2781–2793 (2022).
9. Takeda, H. et al. Structural basis for ion selectivity revealed by high-resolution crystal structure of Mg2+ channel MgtE. *Nat. Commun.* **5**, 5374 (2014).
10. Lunin, V. V. et al. Crystal structure of the CorA Mg2+ transporter. *Nature* **440**, 833–837 (2006).
11. Eshaghi, S. et al. Crystal structure of a divalent metal ion transporter CorA at 2.9 angstrom resolution. *Science* **313**, 354–357 (2006).
12. Guskov, A. et al. Structural insights into the mechanisms of Mg2+ uptake, transport, and gating by CorA. *Proc. Natl. Acad. Sci. USA* **109**, 18459–18464 (2012).
13. Sato, M. et al. Stopped-flow analysis on anion binding to blue-form halorhodopsin from Natronobacterium pharaonis: comparison with the anion-uptake process during the photocycle. *Biochemistry* **41**, 2452–2458 (2002).
14. Wang, T. et al. Deprotonation of D96 in bacteriorhodopsin opens the proton uptake pathway. *Structure* **21**, 290–297 (2013).
15. Caffrey, M. & Cherezov, V. Crystallizing membrane proteins using lipidic mesophases. *Nat. Protoc.* **4**, 706–731 (2009).
16. Yamashita, K., Hirata, K. & Yamamoto, M. KAMO: towards automated data processing for microcrystals. *Acta Crystallogr. D Struct. Biol.* **74**, 441–449 (2018).
17. Foadi, J. et al. Clustering procedures for the optimal selection of data sets from multiple crystals in macromolecular crystallography. *Acta Crystallogr. D Biol. Crystallogr.* **69**, 1617–1632 (2013).
18. Desiraju, G. R. and Steiner, T. *The Weak Hydrogen Bond: In Structural Chemistry and Biology* (International Union of Crystal, 2001).
19. Engelhard, C. et al. Microbial halorhodopsins: light-driven chloride pumps. *Chem. Rev.* **118**, 10629–10645 (2018).
20. Gushchin, I. et al. Crystal structure of a light-driven sodium pump. *Nat. Struct. Mol. Biol.* **22**, 390–395 (2015).
21. Inoue, K. et al. A light-driven sodium ion pump in marine bacteria. *Nat. Commun.* **4**, 1678 (2013).
22. Sudo, Y. et al. A microbial rhodopsin with a unique retinal composition shows both sensory rhodopsin II and bacteriorhodopsin-like properties. *J. Biol. Chem.* **286**, 5967–5976 (2011).

23. Inoue, K. et al. Absorption spectra and photochemical reactions in a unique photoactive protein, middle rhodopsin MR. *J. Phys. Chem. B* **116**, 5888–5899 (2012).
24. Nogly, P. et al. Lipidic cubic phase serial millisecond crystallography using synchrotron radiation. *IUCrJ* **2**, 168–176 (2015).
25. Otwinowski, Z. & Minor, W. Processing of X-ray diffraction data collected in oscillation mode. *Methods Enzymol.* **276**, 307–326 (1997).
26. Jumper, J. et al. Highly accurate protein structure prediction with AlphaFold. *Nature* **596**, 583–589 (2021).
27. Liebschner, D. et al. Macromolecular structure determination using X-rays, neutrons and electrons: recent developments in Phenix. *Acta Crystallogr D Struct. Biol.* **75**, 861–877 (2019).
28. Agirre, J. et al. The CCP4 suite: integrative software for macromolecular crystallography. *Acta Crystallogr. D Struct. Biol.* **79**, 449–461 (2023).
29. Emsley, P. et al. Features and development of Coot. *Acta Crystallogr. D Biol. Crystallogr.* **66**, 486–501 (2010).
30. Meng, E. C. et al. UCSF ChimeraX: tools for structure building and analysis. *Protein Sci.* **32**, e4792 (2023).

Acknowledgements

The x-ray diffraction tests and data collection in this work were carried out with the use of TPS 07A and TLS 15A1 at NSRRC, Taiwan. We thank the experimental facility and the technical services provided by "The Synchrotron Radiation Protein Crystallography Core Facility (SPXF) of the National Core Facility for Biopharmaceuticals (NCFB), National Science and Technology Council (NSTC)" and the "National Synchrotron Radiation Research Center (NSRRC)," a national user facility supported by the National Science and Technology Council of Taiwan (NSTC), Taiwan, ROC.

Author contributions

L.N.K., G.Z.L., T.K., and C.S.Y. designed research; L.N.K., G.Z.L., T.K., J.C.C. and G.Y.L. performed research; L.N.K., G.Z.L., J.C.C., G.Y.L. and C.S.Y. analyzed data; and L.N.K., G.Z.L. and C.S.Y. wrote the manuscript.

Competing interests

The authors declare no competing interests.

Additional information

Supplementary information The online version contains supplementary material available at https://doi.org/10.1038/s41467-025-59795-y.

Correspondence and requests for materials should be addressed to Chii-Shen Yang.

Peer review information *Nature Communications* thanks the anonymous reviewers for their contribution to the peer review of this work. A peer review file is available.